Development of a 3D finite element model at mesoscale for the crushing of unidirectional composites

Florent Grotto, Samuel Rivallant, Christophe Bouvet

Development of a 3D finite element model at mesoscale for the crushing of unidirectional composites: Application to plates crushing

Florent Grotto, Samuel Rivallant, Christophe Bouvet *

Université de Toulouse – Institut Clément Ader – ISAE-SUPAERO, INSA, IMT Mines Albi, UPS – Toulouse, France

Keywords:
Crashworthiness
Energy absorption
Finite element analysis
Carbon UD laminate

A B S T R A C T

This paper presents the development of a new 3D finite element model for the simulation of UD composites materials under crushing, at the mesoscale. It is based on the Discrete Ply Model (DPM), enhanced with a new damage law to represent compression at constant stress due to localised crushing and its propagation from one element to another. The model aims to take into account the various damage types involved in UD laminates during crushing and the associated absorbed energies: delamination, splitting, ply rupture in tension or bending, compression due to localised fragmentation and friction. The model is confronted with experimental results obtained on laminated plates crushing: not only global metrics (force, energy absorbed…) but especially key morphological aspects of the crushing front (delamination lengths, splaying, number of plies under localised crushing, debris wedge…) thanks to high speed camera pictures.

1. Introduction

As composite is now widely used in the field of transport (automotive, aerospace, railway and shipbuilding industries) and authorities impose high requirements in terms of security, composite crashworthiness is a key issue in this domain. Concerning energy absorption, crash boxes made of composite materials, or equivalent structures, can be more efficient than metallic ones [1,2], or really inefficient in case of a bad design. Indeed, design parameters such as material choice, fibre orientation [3], stacking sequence [2], absorber geometry [4] or trigger mechanism [5] are of first importance, but experimental campaigns to identify the good ones are both costly and time-consuming. That is the reason why researchers are more and more interested in virtual testing for crashworthiness. One of the major difficulties in the simulation of energy absorption in composite materials is the complexity of mechanisms involved in composite crushing: from the initiation of failure to the possible complete rupture of the material, including kinking [6] debris interaction [7], friction [8], material compaction… Depending on the expected level of accuracy and computational efficiency, different models were developed in recent decades.

The first finite element simulations of composite crushing appeared at the end of the 1980s [3]. Since then, thanks to a better understanding of the crushing behaviour of composite and improvements in computing power, simulation of crushing has evolved considerably, especially in the past ten years [9]. Models can be classified in two categories: non predictive and predictive ones. For example, models based on CZone add-on from Abaqus [10,11] are not expected to be able to predict the crushing force as the average crushing stress of the laminate is an input of the model and is known to be strongly dependant on the material, the stacking sequence, and the geometry [2,4]. In the same vein, the use of only one element in the thickness of a laminate [12–15] cannot represent the complex crushing front with delamination and splaying observed in most of the crushing tests, even if the calibration of the damage law parameters sometimes allows to reach a quite good level of force and energy. On the other hand, models at microscale or based on a very fine representation of the material always lead to prohibitive computation times [16] for real structures simulations. That is why a representative simulation of crash for a structure or subcomponent [17] is still an issue today, even if some progress has been made in terms of multiscale approach [18].

Thus, most authors agree today that for a predictive model, it is necessary to have a model architecture including at least a set of sub-laminates separated with delamination interfaces such as cohesive zone elements or tiebreak interfaces [19–21]. In this paper, we will focus on this class of models.

Concerning the material model, of course, the choice of the model depends on the type of composite material used, but models which can represent both a realistic geometry of the crushing front and a good level

* Corresponding author.
E-mail address: christophe.bouvet@isae-supaero.fr (C. Bouvet).

https://doi.org/10.1016/j.compstruct.2022.115346

of energy dissipation all include a propagation of damage after failure onset, most often related to an energy release rate for fibre tension and compression failure, and element deletion.

As it is available in LS-Dyna software, the MAT54 enhanced composite damage model is often used in the simulation of crushing of tubes [22–27]. It produces quite good results, with an overall good representation of petals inside and outside the tubes, but as written in [23], there are too many non-physical parameters to identify and calibrate that the field of application is quite limited, and such a model cannot be described as predictive.

Sokolinsky et al. [21] proposed a constitutive model for fabric plies based on continuum damage mechanics, taking into account energy release rate for fibre failure in tension and compression through a damage evolution law including a characteristic length to limit mesh dependency. They also added a plastic shear model for the in-plane shear behaviour. The same kind of approach is used by Chiu et al. [28] for unidirectional plies and Liu et al. [29] for hybrid unidirectional and woven CFRP, showing quite good results on both the force/time curve and the front morphology. McGregor et al. [8,30] implemented and applied the CODAM model to the crushing of braided composite tubes. This model also includes a plateau stress to represent the compression bearing behaviour. Rondina et al. [31] recently implemented and compared two models to simulate the crushing of corrugated plates made of unidirectional CFRP. The first model is based on the Ladevèze continuum damage model [32], while the second is the Waas-Pineda model [33]. They obtained good results in both cases, but the identification of parameters is more complex for the Ladevèze model. The force/displacement curves also show great oscillations before filtering in the plateau force. Oscillations width corresponds to element length, which certainly comes from a lack of softening in the models. Costa et al. [6] recently developed a new fibre kinking model for crushing application that manages to catch the local morphology of the crushing front of a carbon NCF laminated plate. All these recent results are encouraging in finding solutions for fine crushing response prediction.

This paper presents the development of a new finite element model for the simulation of UD composites materials under crushing, at the mesoscale. It is a 3D model based on a previous pseudo-2D model developed to represent the crushing of composite laminated plates [34]. It aims to take into account all damage types in UD laminates under crushing and the associated absorbed energies: delamination, splitting, ply rupture in tension or bending, compression at constant stress due to localised fragmentation [35] and friction. The model is discussed and validated from experimental results on laminated plates made of 0° and 90° UD plies [36]. Both scalar data (force, energy…) and mechanisms (including chronology) are analysed. The choice of plates as experimental validation tests was made to have more information during crushing tests: the sides of the plates can be filmed during the test, giving location and evolution of delamination, splaying plies, localised crushing, debris wedges… In plates, there is also no hoop effect as can be found in closed sections, which allows to numerically validate the stability of plies undergoing localised crushing (pure compression) and the delamination technics used to represent delamination extent when splaying occurs.

2. Experiment

2.1. Test set-up and experimental data

Experimental tests results from previous studies [34,36] are used to develop and validate the numerical model. The unique specimen type we are focusing on is a 16 plies laminate $[(0°/90°)_4]_s$ made of T700/M21 carbon epoxy UD prepregs, with a 0.26 mm ply thickness. The specimen is a $160 \times 60 \times 4.16$ mm^3 flat plate, with a 45° chamfer trigger at the tip to initiate damage (Fig. 1). The chamfer is machined cautiously with a circular diamond saw blade and controlled visually to be sure that there is no damage before the test. In accordance with the common convention, the 0° direction matches the 160 mm length of the specimen (i.e. crushing direction).

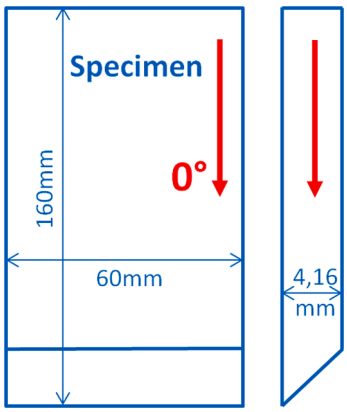

Fig. 1. Specimen geometry.

The experimental set-up (Fig. 2) vertically guides the specimen to crash into a horizontal base plate, throughout the first 100 mm of its 160 mm length. The specimen is held by a cylinder that pushes the plate inside the test device (more details in [37;38]). Eight experimental tests from [36] are used in this study to validate the numerical model. The eight specimens have the same size and stacking sequence as presented above. Only the loading changes: two static tests and six dynamic tests. Three different initial speeds were considered for dynamic tests: 2, 5 and 9 m/s (two tests for each speed).

Static tests are performed using a universal testing machine, the cylinder being fixed to the crosshead. Dynamic tests are performed using a drop tower with a 36 kg falling weight, the cylinder being fixed below the mass. The crushing force is measured thanks to a 120 kN Kistler piezoelectric load sensor fixed at the bottom of the cylinder, just above the specimen. In statics, the displacement is given directly by the testing machine. In dynamics, it is calculated by double integration of the acceleration (proportional to the crushing force). The initial speed (speed at impact) is measured with a Laser sensor. Thus, force–displacement curves can be computed. One of the two dynamic tests at each speed are presented in Fig. 3. High speed cameras are also used to visualize macroscopic fracture mechanisms (Fig. 4) through the visualization hole (Fig. 2). The image acquisition speed is 20,000 frames per second in dynamics, with a 40 pixels per mm resolution, whereas the force acquisition speed is 1 MHz.

2.2. Evolution of specimen morphology during crushing

To understand the evolution of a crushing, it is important to consider both the force and the mechanisms involved in the damage process. High speed camera allows the description of macroscopic fracture mechanisms throughout testing. In agreement with tests videos, a reference side-view of the specimen is set, with the tip of the 45° trigger of the specimen on the left. Further explanations and figures will all abide by this convention.

The force–displacement curves (Fig. 3), as well as evolutions of specimens fracture morphologies (Fig. 4), show two main phases: a high and short peak preceding a long plateau with oscillations, clearly defining an initial phase and a steady phase. The transition phase refers to the unclear phase between the peak and the plateau.

2.2.1. Initial main delamination

On the first moments of crushing, damage is localised at the tip of the plate. Only plies on the left are crushed, progressively, and delamination is limited to a few millimetres height. Then, after around 4–5 mm displacement, a main delamination occurs brutally all the way up to the

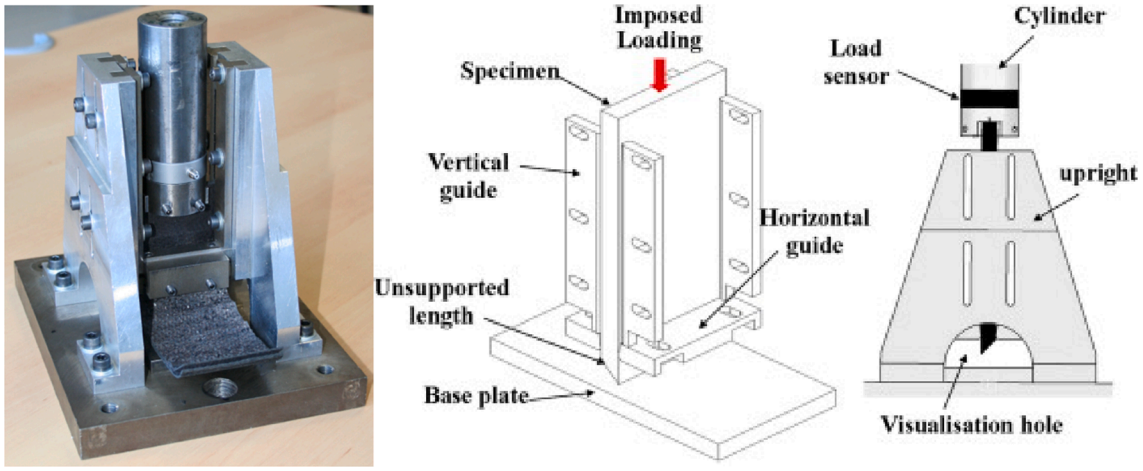

Fig. 2. Experimental test set-up for laminated plate crushing. Photo with a crushed specimen and CAD drawings (left: set-up without uprights to see horizontal and vertical guides - right: set-up with uprights and cylinder holding the specimen).

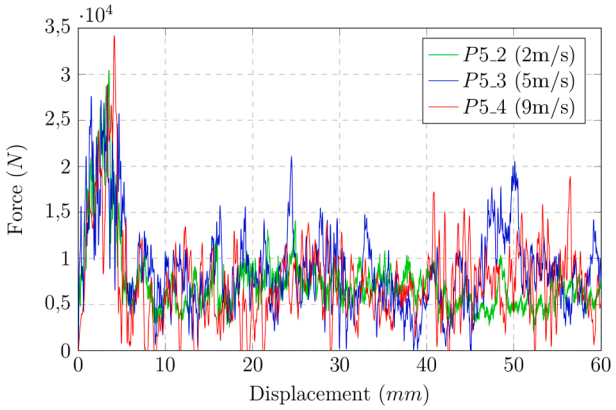

Fig. 3. Experimental force–displacement curves for three initial crushing speeds.

20 mm unsupported length of the specimen (Fig. 4-a), delimited by the horizontal guides. The position of this delamination can vary from a test to another but tends to mainly appear in the centre-right of the specimen, and often adjacent to the central 90° double ply. It is shown by vertical marks in Fig. 5. This main event matches with the end of the force peak and a brutal drop of crushing surface.

2.2.2. *Main column*

After the transition phase, a main steady vertical column appears during the crushing (Fig. 4-b), usually to the left of the central double 90° ply and is quite stable during the steady phase. The horizontal lines in Fig. 5 represent location and width of the column. The number of plies in this column is not exactly the same for all the tests (from four to eight) and can slightly change during a given crushing. Dotted lines in some of the tests show these temporary changes.

This crushing column gives two main distinct fracture modes, described by [35]. Firstly, exterior plies of the main column suffer intra-laminar ply failures, generating repetitive macroscopic fragments about 3–5 mm long. Secondly, the inner column fractures were identified as micro-buckling of fibres in 0° plies and multiple shear micro-cracks in 90° plies, leading to the definition of the ply Mean Crushing Stress (MCS) by [35], which is responsible of the main part of the energy dissipation and of the global force level.

2.2.3. *Splaying*

Splaying is the progress of macroscopic delamination opening and plies bending during crushing. Macroscopic delaminations form bundles of splaying plies: one bundle on each side of the main column (Fig. 4-b). The two splaying bundles each contain a superficial 0° ply and may contain several 0–90° ply couples. Splaying couples always bend plies in the same way: the 0° ply in tension and the 90° ply in compression.

Delamination height of splaying plies reaches quite stable levels,

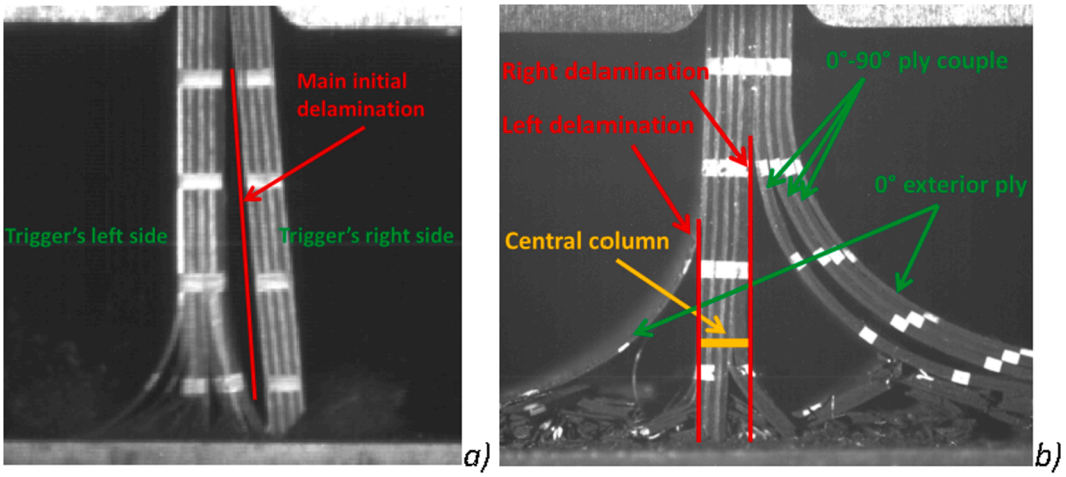

Fig. 4. Typical specimen morphology during the crushing: a) main delamination after peak force - b) morphology during the steady phase.

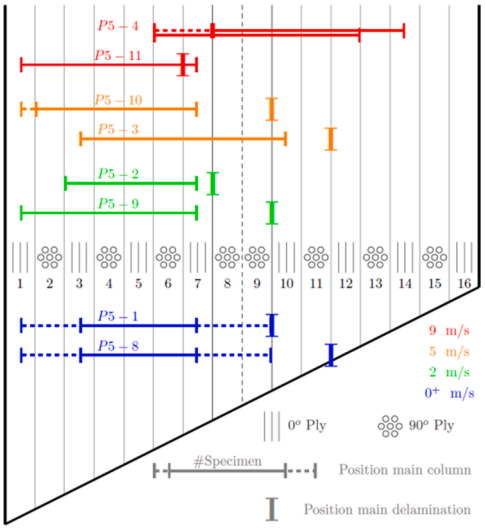

Fig. 5. Position of the main crushing column and the main initial delamination for each specimen tested.

typical of the steady phase. For each test, the left and the right delamination delineating the main column (Fig. 4-b) are respectively stabilized around 9 mm and 15 mm heights.

2.2.4. Variability

Various aspects of the macroscopic morphology of the specimen shows variability between tests, such as the position of the main delamination, the position and width of the main column, macroscopic fragmentation occurrences. The P5-4 specimen did not even properly generate a distinctive main initial delamination neither a stable main column (Fig. 5).

An average scenario appears with important but reasonable variability on the force–displacement curves and the morphologies evolutions. For experimental–numerical confrontation, this experimental variability must be put into perspective.

3. Numerical model

3.1. Discrete ply model

The Discrete Ply Model (DPM) is a *meso*-scale finite element model for unidirectional laminates, using Abaqus Explicit solver and user material law, developed at ICA for a decade [39,40,41]. Regarding specimen fractures, most fracture mechanisms happen at the scale of the ply (delamination, fragmentation, matrix cracking, splaying) therefore the mesoscopic scale of the model suits this application. DPM represents delamination and matrix cracks as discrete fractures, thanks to COH3D8 cohesive elements surrounding C3D8I volume elements (Fig. 6). The C3D8I formulation of volume elements is important to respect bending stiffness of splaying plies since each ply is meshed with only one element through the thickness.

The failure and separation parameters used for these cohesive elements are listed in Table 1. They are the classical transverse tensile strength, in-plane shear strength and toughness in mode I, II and III (assuming mode II and mode III parameters are the same). They are identified from standard tests, and a correction is added to toughness parameters to fit the curvature and delamination length of given splaying plies (see 4.2.2).

3.1.1. Matrix cracking

The failure criterion for matrix cracking is not directly calculated in corresponding cohesive elements but in neighbouring volume elements to avoid stress concentration in cohesive elements (Fig. 6). When the

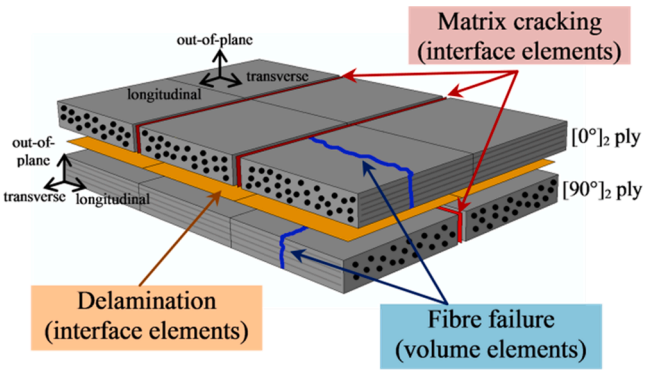

Fig. 6. DPM meshing principle: element types and associated damage.

Table 1
Material properties used to numerically model T700/M21 laminate.

Parameter	Unit	Symbol	Value
Elasticity			
Density	$kg.m^{-3}$	ρ	1600
Young Modulus			
Longitudinal traction	*GPa*	E_l^T	130
Longitudinal compression	*GPa*	E_l^C	100
Transverse	*GPa*	E_t	7.7
Shear Modulus	*GPa*	G_{lt}	4.75
Poisson ratio	–	ν	0.3
Fibre failure			
Longitudinal damage initiation			
Traction			
Compression	–	ε_0^T	0.018
Toughness	–	ε_0^C	−0.0125
Traction			
Compression	$\frac{N}{mm}$	G_f^T	80
Interface fracture	N/mm	G_f^C	30
Transverse tensile strength	MPa	S_{nt}	60
In-plane shear strength	MPa	S_{lt}	110
Toughness mode I	N/mm	G_I^{del}	0.5
Toughness mode II and III	N/mm	$G_{IIorIII}^{del}$	1.6
Miscellaneous			
Mean Crushing Stress	MPa	σ_{MCS}	140 & 250
Friction Coefficient	MPa	f	0.14
Max. Transverse expansion	N/mm	$\Delta\varepsilon_{zz}^{p,max}$	0.8

Hashin stress criterion is reached (Equation 1), the local matrix cracking cohesive element is deleted.

$$\left(\frac{\langle\sigma_t\rangle^+}{Y_T}\right)^2 + \frac{{\tau_{lt}}^2 + {\tau_{tz}}^2}{{S_L}^2} \geq 1$$

$\langle\sigma_t\rangle^+$: transverse tensile stress, τ_{lt} and τ_{tz}: shear stresses, Y_T: transverse failure stress, S_L: Shear failure stress

Equation 1: Hashin stress criterion for matrix cracking

Naturally if the criterion is reached in a volume element then the two neighbouring matrix cracking cohesive elements should be deleted. To avoid this double cracking, the Hashin criterion is computed for each 8 integrations point of the C3D8I volume element and the cohesive element only takes into account the neighbour integration point as described in Fig. 7.

3.1.2. Delamination

Delamination is modelled thanks to dedicated cohesive elements (Fig. 6). A linear softening stress versus displacement is implemented to represent the dissipated energy, with respect to mode I, II, III stress

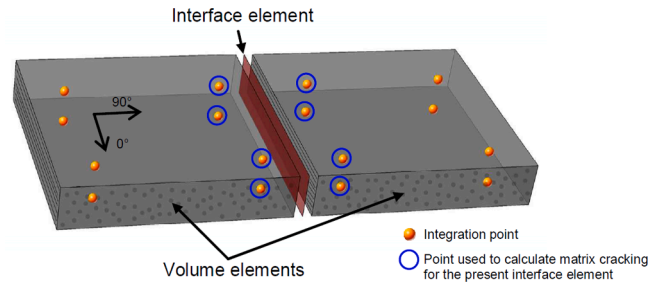

Fig. 7. Communication between a matrix cracking element and specific neighbouring integration points of neighbour's volume elements.

initiation thresholds and critical energy release rates. Once a cohesive element dissipates the entire critical energy release rate, it is deleted.

3.1.3. Fibre failure

Fibre failure is modelled continuously with a linear softening stress versus displacement, with respect to the strain threshold damage initiation and the critical energy release rates (Fig. 8-a). As described with Equation 2 we represent the fibre breakage, which is a brutal surface phenomenon, as the continuous damaging of a volume. The size of the element is thus considered in the energy calculation to avoid mesh-dependency effect.

$$\int_{Volume}\left(\int_{0}^{\varepsilon_1}\sigma\cdot d\varepsilon\right)dV = S\cdot G_{Ic}$$

Equation 2: For fibre failure, accordance between the energy dissipated in a volume element and the critical energy release rate on the cross-section of the element

At each time step, a single damage variable is computed for a whole element (Fig. 8-b) such as the stresses (at 8 integration points) linearly decrease and the critical energy release rate is finally dissipated for the whole element.

The tension and compression are distinguished as we use different values of strain threshold (ε_0^T and ε_0^C the strain damage initiation thresholds, Table 1) and different critical energy release rate ($G_{Ic}{}^T$ and $G_{Ic}{}^C$) but both traction and compression history are aggregated in the unique damage variable of the element. Such implementation was meant to describe alternated tension–compression histories and the bending of a single element which generate positive strains on one side and negative strains on the other side at the same time.

3.2. DPM adaptation for crushing

The DPM was first adapted by [34] to represent the plate crushing, but only in a pseudo-2D model. Relevant phenomenon resulting from micro-fractures – such as fibre's micro-buckling and matrix micro-cracking generating local crushing and wedges as described by [35] – are represented by homogenous equivalent behaviours and volume element deletion.

3.2.1. Front softening

The Free Face Crushing concept was implemented as a front softening for damage-initiated extremities. The crushing and inside ply fractures ongoing, front softening needs to be propagated to new extremities continually generated. Thus, high damage values are automatically applied to deleted elements' neighbours as illustrated on Fig. 9.

3.2.2. Debris accumulation

The debris accumulation during crushing induces a local transverse expansion, critical to initiate splaying and to initiate the superficial fragmentation of the main column. Therefore [34] introduced a pseudo-plastic deformation in the laminate thickness direction to represent the local expansion of 90° plies extremities (Equation 3). Thus, an element under transverse compression is keeping a constant volume until a −80% compressive nominal strain.

$$\Delta\varepsilon_{zz}^{p} = \begin{cases} -\Delta\varepsilon_{tt}^{p} \; if \; \Delta\varepsilon_{zz}^{p} < 0.8 \\ 0 \; else \end{cases}$$

Equation 3: Modelling of debris accumulation with a pseudo-plastic out of plane strain, opposite to the transverse plastic strain

3.2.3. Deletion smoothing

The use of discrete element deletion to represent continuous crushing allows to describe the mass loss due to continuous debris evacuation during crushing but generates a peak of compression release. Israr et al. [34] introduced an artificial linear stress decrease preceding deletion under compression to smooth the stress release peaks (Fig. 11).

3.3. Geometry

In this study, the model is adapted to 3D simulations. The numerical geometry of the specimen matches the experimental specimen: same ply stacking, same thickness and same 45° chamfer trigger at the tip (Fig. 10). But the simulated specimen is shorter and narrower (50 mm length instead of 160 mm and 8 mm width instead of 60 mm) to focus on the first 30 mm of crushing length and to keep reasonable computation

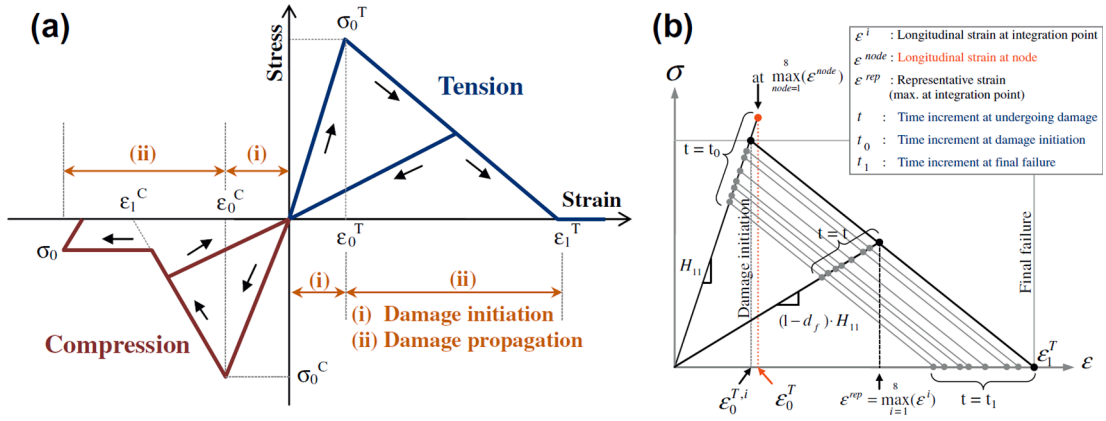

Fig. 8. Modelling of fibre failure (a) taking into account traction and compression (b) computing final deformation of the linear softening so the whole volume element (C3D8I) actually dissipates the critical energy expected.

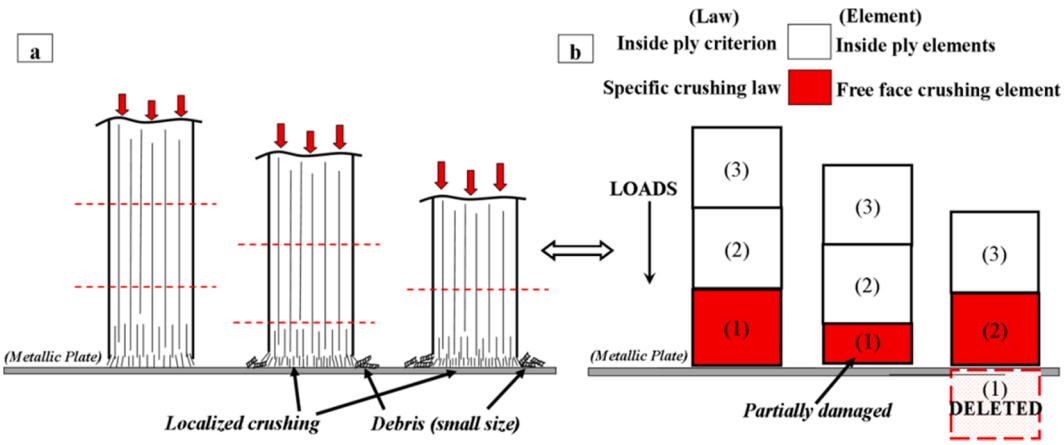

Fig. 9. Illustration of column of elements crushing and front softening communication (34).

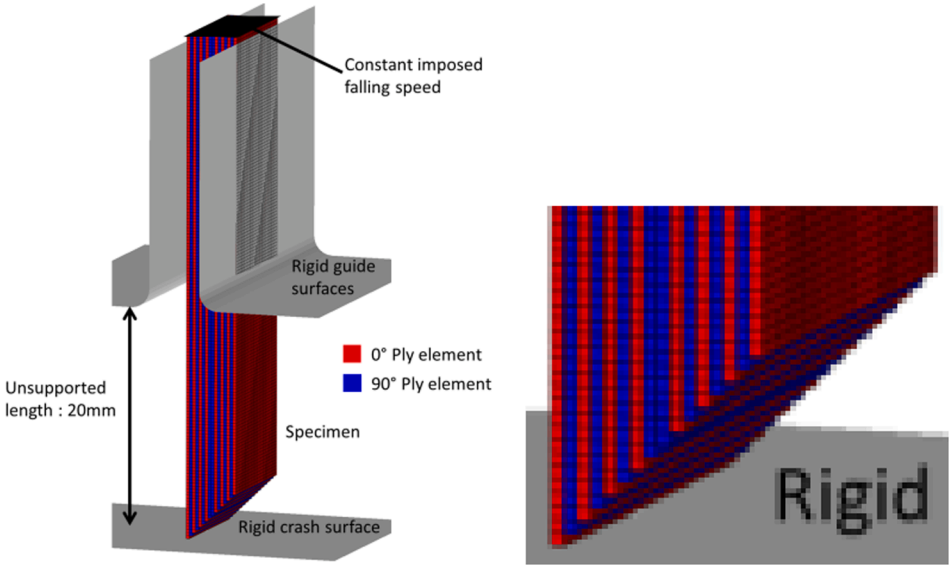

Fig. 10. FEM discretization of the specimen geometry (full model and chamfer detail).

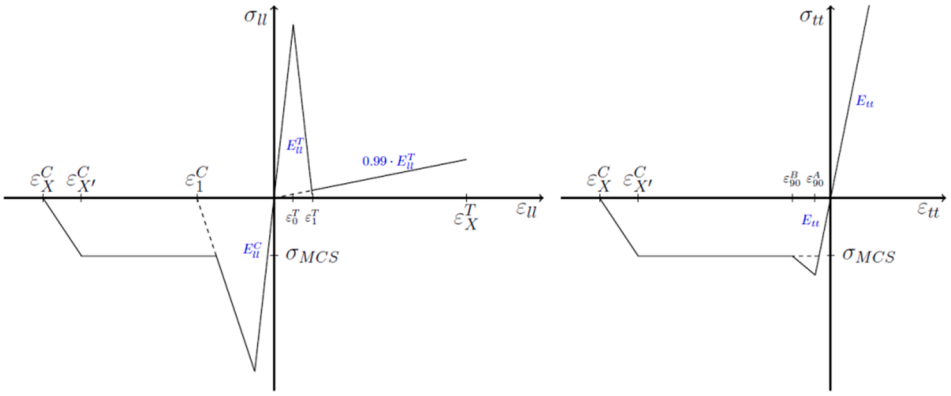

Fig. 11. Longitudinal and transverse behaviour law (arbitrary scale).

durations.

It is possible to reduce the specimen length in the simulation because the guides impose a no rotation condition of the upper part of the specimen and it has been observed during experiments that damage - delamination or ply failure - never occurs or propagates higher than the horizontal guides. A 50 mm length specimen in the simulation assures that even after 30 mm crushing 20 mm of the sample remain between the guides, enough to impose the no rotation condition. It has also been observed that the crushing front morphology shows invariance in damage along width, thus it is assumed that the width can be reduced in the simulations. 8 mm were chosen so that there are enough elements in the width (16 elements with the 0.5 mm element size used). Loads levels

in the model can then be compared directly to experimental data using the width ratio. Analytical rigid surfaces are used to represent boundary conditions with respect to experimental geometry (Fig. 10). Experimental falling speeds during crushing decrease very little thanks to the 36 kg falling weight, therefore a simple constant speed is imposed at the top of the simulated specimen. Duong et al. [36] have shown testing low dependency to initial crushing speed so a 10 m/s constant speed is imposed in numerical simulations, to be compared with 2 m/s, 5 m/s and 9 m/s testing.

Israr et al. [34] have developed this numerical simulation geometry, limited to a pseudo-2D purpose: only one element and blocked displacement in the width direction. Further objectives of this study are to develop full 3D simulations, notably with 45° plies, without width-direction invariance. However, this pseudo-2D geometry (80 mm length, 0.25 mm width) is still used for obvious computation time purposes during developments but the full 3D geometry turns out to be necessary to get results representative of the experiments.

We use a homogenous ($0.5 \times 0.5 \times 0.26$ mm) rectangular meshing so that we only have one element in each ply thickness. Computations on a 36-cores supercomputer last 11 h for the simulated 3D geometry (0.25e-8 s step time, 100 000 elements).

Israr et al. [34] used triangular volume elements to complete the rectangular meshing in the 45° chamfer and fit the real geometry. We found that these triangular elements have no relevant effect, so we decided not to mesh them thus to let a stair-shaped front of the chamfer (Fig. 10, detail).

3.4. Past results limitations

Israr et al. [34] focused on pseudo-2D simulations on the first 20 mm of crushing for the dynamic testing. The initial peak force was quite well represented but the crushing in the plateau phase was highly unstable thus generated major drops to zero in the force plateau which were not observed during the experiments and led to underestimate energy absorption.

4. Application

4.1. New developments in the numerical model

4.1.1. Materials laws unification

Israr et al. [34] chose to describe 0° and 90° with separated specific material laws. This study aims for a unique material law, so that this model could later naturally describe any ply orientation. Therefore the Israr et al. version of the DPM was improved to unify both oriented material laws and also the specific "localised crushing law" (compression bearing at constant stress level, localised at the tip of the ply) with the "inside ply law" (failure mainly due to bending).

Fig. 11 illustrates the new material law, with different longitudinal and transversal behaviours. Longitudinal and transverse compressive laws are very similar: an initial stress peak is followed by a stress plateau (corresponding to the Mean Crushing Stress) and finally the stress progressively drops to zero before deletion. The longitudinal tensile law describes an elastic part then a linear decrease during damaging (to dissipate fibre failure energy) but a residual stiffness is left to avoid unrestrained elements expansion. The three shears have elementary linear elastic laws.

4.1.2. Stress waves robustness

Such crushing simulation generates strong stress waves, both physical and numerical (element deletion), which damage and fracture criterions are very sensitive to. Moreover, given the regular meshing, all lined-up elements at the crushing front are deleted almost simultaneously during crushing which generates strong repetitive stress waves. The default numerical viscosity of Abaqus Explicit is used, which is not enough to smooth the stress waves. To avoid unintentional alteration from these stress waves, especially in the case of unrealistic numerical peak forces due to element deletion, all deletion and damaging criterions are based on temporally filtered strains and stresses.

4.1.3. Excessive distortions robustness

During those crushing simulations, many elements excessive distortions occurred and caused fatal errors. Elements excessive distortions mainly appear during element crushing where the nominal strain goes down to -0.95 or even less. On the contrary to the pseudo-2D geometry, the 3D geometry is not artificially guided to avoid width-direction displacements, so distortion of element tends to be less inhibited.

Mesoscopic and macroscopic shear have little relevance for this specific application, so shear modulus damaging is fully disabled to avoid over-distortion of strongly damaged elements. Even though it dissipates energy, the "Distortion Control" tool of Abaqus Explicit is used to reduce excessive distortion of volume elements.

Excessive element distortion fatal errors still exceptionally happen so a negative Jacobian distortion criterion is implemented in the behaviour law to delete critically distorted elements before they generate a fatal computation error. It has been checked that deletion of these elements has very few influence on the global behaviour, especially in terms of energy dissipation.

4.1.4. Cauchy stress correction

The Mean Crushing Stress observed when a ply is crushed in a localised fragmentation mode is defined as a constant nominal stress, whereas finite elements naturally work with Cauchy stresses. Poisson effects are usually weak enough to neglect the difference between Cauchy strain and nominal strain but the transversal expansion implemented generates a considerable Cauchy/nominal difference.

A simple correction is applied, function of transverse strain, so that elements give the nominal stress expected for the Mean Crushing Stress. Fig. 12 shows the effect of the nominal stress correction on the force resulting from the crushing of a single column of elements. The expected constant force due to the MCS is represented by the green line.

4.1.5. Artificial initial main delamination

The initial main delamination observed in experiments after a few millimetres of crushing (Fig. 4-a) does not spontaneously appear in numerical simulations (with the dynamic MCS, see later). As explain in the next section, it is a crucial step to the formation of the main column and the evolution of the crushing morphology. Thus, simulations are run in pair: normal specimens and pre-delaminated specimen simulations (10 mm delamination height on right 0°/90° interfaces) to emulate the splaying initiation effect of the main initial delamination.

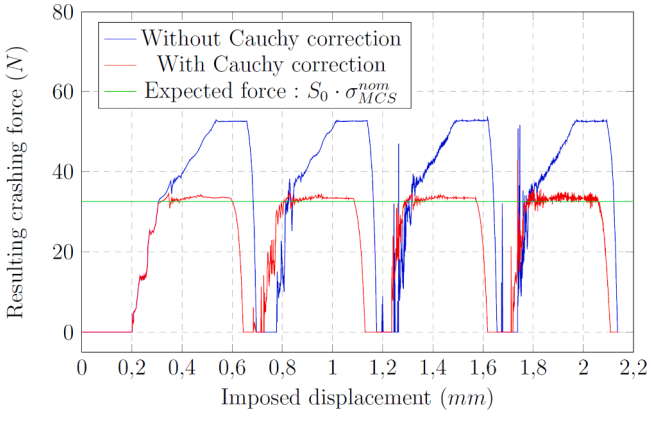

Fig. 12. Effect of Cauchy stress correction on the force due to the crushing of a column where a constant nominal stress is expected.

4.2. Material constants identification

Material values discussed below are reported in Table 1.

4.2.1. MCS (Mean Crushing Stress)

The MCS value was identified for quasi-static tests by [35] but due to experimental difficulties (high-speed cameras resolution, force signal / camera pictures synchronisation…), a precise identification of the dynamic value for MCS has not yet been done. However, the dynamic MCS is roughly identified as 140 MPa for this study (instead of 250 MPa for quasi-static tests) using the same method as [35] on the P5-9 test.

This speed effect driving the value of the MCS is here identified to be a key to represent both initiation phase and steady phase of the experiment. On one hand, the initial main delamination appears in simulations only if we use the quasi-static value of the MCS, which is critical to later describe the right morphology during the steady phase. On the other hand, during the steady phase it is necessary to use the dynamic value of the MCS to describe the right force plateau and the right morphological behaviour.

Hence, we launch simulations in (another) pair: with the quasi-static MCS or with the dynamic MCS. The first is expected to be representative of the experiment initiation phase and the second of the steady phase. Unless otherwise specified, we use the dynamic MCS.

4.2.2. Delamination and friction

Israr et al. [34] identified the friction coefficient comparing experimental and numerical bending curves of splaying plies on the base plate. The same method is used to identify simultaneously the friction coefficient and the correction of delamination strength values on two morphological criterions: the curvature of splaying plies (Fig. 13-a-b: red ellipses) - as in [34], and delamination heights around the main column (Fig. 13-c-d: red lines). A parametric study of the parameters f, S_{nt}, S_{tt}, G_I^{del} and G_{II}^{del} is launched, for crushing simulations, varying parameters around 0.15 for f and around the values identified from tensile, DCB and ENF tests for cohesive elements parameters. Curvatures and delamination heights are compared for a few numbers of pictures from experiments and the set of parameters that gives the best compromise is chosen.

The friction coefficient identified is very close to the one identified by the previous method: 0.14 instead of 0.15. Delamination strength values (i.e. stress initiation thresholds and energy release rates for mode I and II) are 10% above the ones characterized by specific experimental testing (DCB for mode I and ENF for mode II), which measurement accuracies are worse than 10%.

4.2.3. Fibre failure energy dissipation

As it is implemented so far, the Discrete Ply Model does not allow to properly describe the bending failure of a ply since we do not describe shear damaging which may induce element distortion issues. Local failure during ply bending is critical to be able to represent the splaying-fragmentation shift of middle plies and the stability of the expected morphology. We have artificially reduced the fibre failure critical energy to 85% of the previous studies values [34,41] so that the model can localise the bending damaging on a single element and finally break the over-bended ply. Anyhow for this plate crushing application, the fibre failure energy is negligible compared to the localised crushing dissipation energy.

5. Results and discussion

Unless otherwise specified, results of computation shown here are obtained with default parameters: dynamic Mean Crushing Stress (140 MPa), without pre-delamination and 3D (not pseudo-2D). The crushing forces on the plates are linearly extrapolated to be compared to the experimental results on 60 mm width specimens.

5.1. Morphological results

5.1.1. Pseudo-2D simulations

Pseudo-2D (Fig. 16) simulations show morphologies similar to 3D simulations (Fig. 14) but also notable differences deteriorating the overall stability. Firstly, delaminations are higher in pseudo-2D simulations forming a longer main column, leading to repeating breakage by buckling of the main column. Picture in Fig. 16 is taken at a moment when, after buckling and failure, the main column is no more in contact with the base plate, and thus the crushing force is close to zero. Secondly, local damages are averaged along the width of a 3D geometry, giving a better stability than a pseudo-2D geometry.

The poor stability of the pseudo-2D geometry, along with the high quasi-static value of the Mean Crushing Stress, are the two main reasons of the lack of stability in Israr et al. simulations [34] leading to repeated force drops to zero instead of a steady plateau phase.

5.1.2. Initial main delamination

In numerical simulations the initial main delamination, observed during experiments, does not appear when using the dynamic value of the Mean Crushing Stress but can appear with the quasi-static value. The artificial initial main delamination deliberately interferes with the morphology progress during the initiation phase so that the simulated

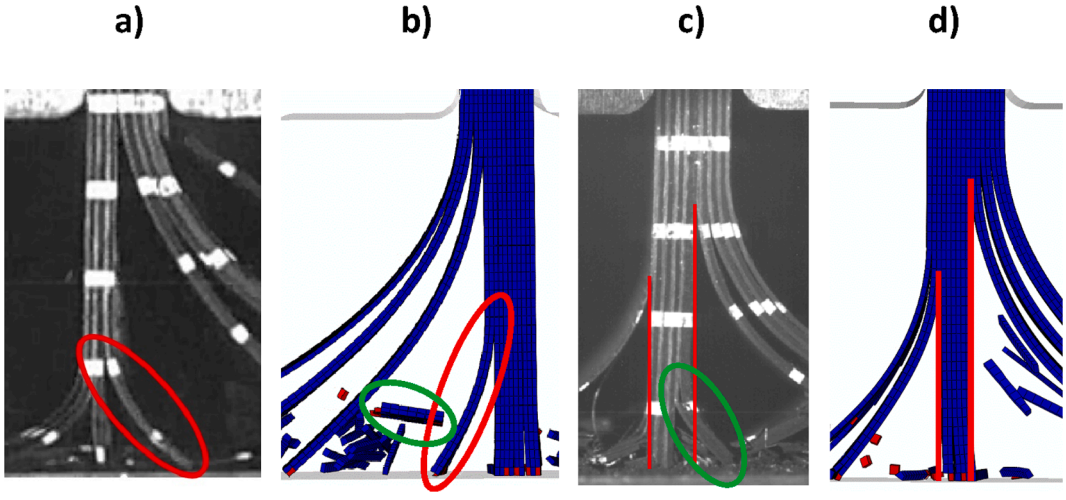

Fig. 13. Identification of coefficients based on simulated morphology. a)-b) experimental and simulated bending curvature of splaying plies c)-d) experimental and simulated delamination height of the main column.

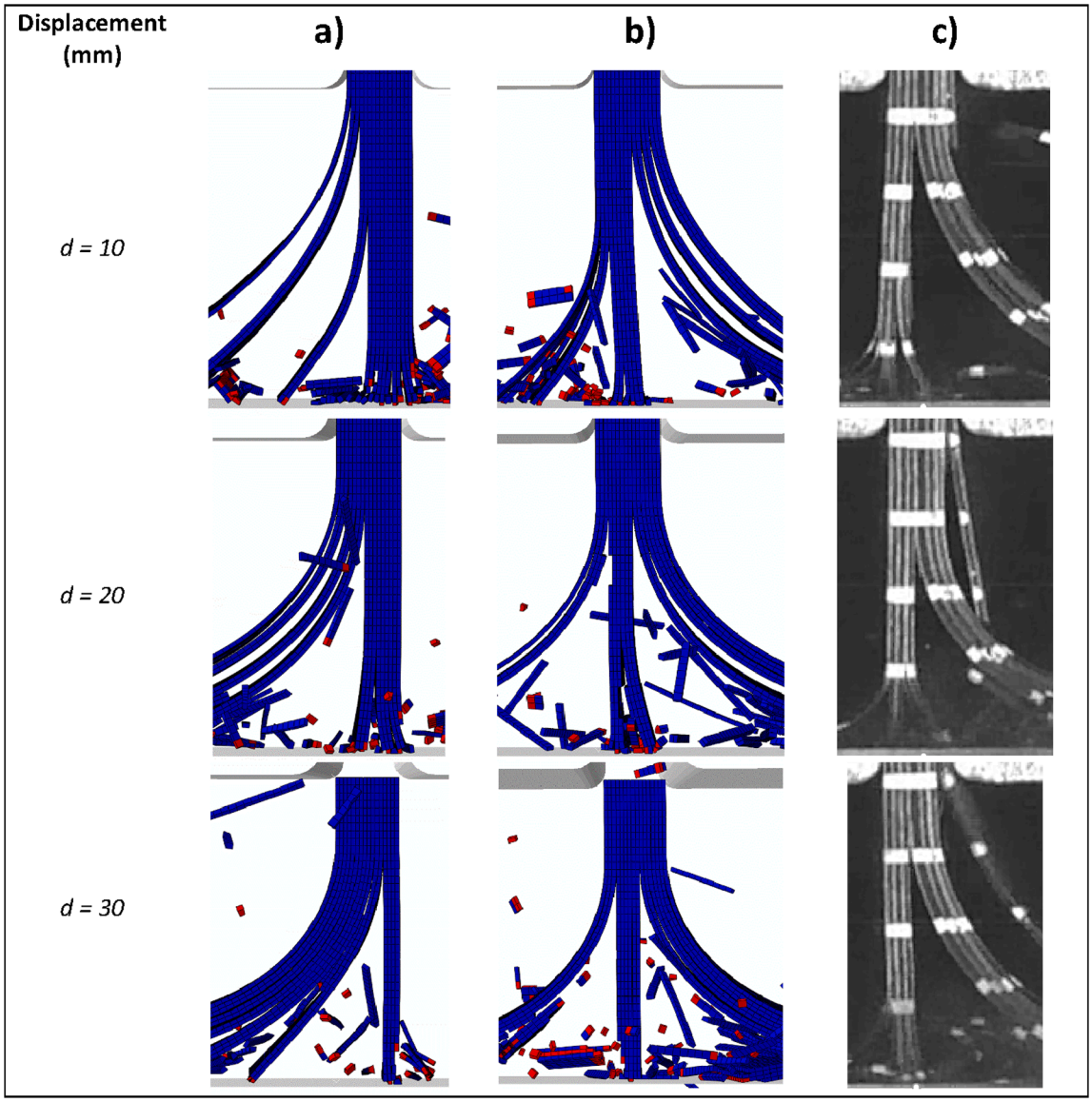

Fig. 14. Comparison of crushing morphologies at specific displacements, 3D model with MCS = 140 MPa - a) simulation without artificial delamination, b) simulation with artificial delamination, c) P5-9 experiment.

morphology is rectified for the permanent phase.

5.1.3. Main column

The main column naturally appears on the right side on numerical simulations (Fig. 14a) but appears and stays on the left side – like in experiments – when applying the artificial main initial delamination (Fig. 14b). Main columns on the left tend to be more stable than main columns on the right, i.e. less prone to generate macroscopic buckling-fracture of the main column and thus drops to zero in the force curves.

Extern plies of the centre column regularly generate macroscopic fragments (about 4 mm long) due to macroscopic bending fractures ("inside ply fragmentation": green ellipses in Fig. 13), as it was described for experimental tests.

5.1.4. Splaying

In all configurations, like in experimental tests, simulated morphologies show splaying bundles holding a superficial 0° ply and several 0–90° ply couples. In the bending couple, the 0° ply is in tension and the 90° ply is always in compression, as matrix cracking does not allow such traction levels for 90° plies.

Left and right delaminations along the main column give heights matching experimental observations (red lines in Fig. 13), as delamination strengths and the friction coefficient were identified for this purpose.

5.2. Analysis

Let us remind that the morphology of the specimen - roughly summarized as splaying plies, fragmentation plies and MCS plies – is fundamental to get the right number of MCS plies, which gives most of the resulting force and thus most of the dissipated energy. Hence, the description of the morphology and its stability is important in the energy dissipation context of this study.

5.2.1. Rows element deletions

The crushing of a column of elements generates quasi-periodic element deletions thus important drops and peaks on the force curve, as seen in Fig. 12 for a single column. Drops are linked to the maximal authorised strain in crushing. It is an expected limit of Finite Elements when trying to represent a continuous crushing. The same effect and

consequences appear on the crushed main column where elements are quasi-simultaneously deleted by rows, and is visible on the global crushing force curve as the force is directly related to the number of crushed plies. The 0.5 mm length of element is clearly visible in the regular force drop occurrence in Fig. 15. Therefore readers may focus on the upper limit envelope of these oscillations to estimate the actual force levels meant to be represented: averaging the level of the force plateau and the slope before the peak would lead to an underestimation. That is why force curves shown in this article are just very slightly filtered, to remove only very high frequency oscillations and make curves readable.

Fig. 15 shows overall consistency of the force plateau level between the 3D simulation and the experiment, even if the simulated curve indicates higher variability due to a less stable main column after 15 mm displacement.

5.2.2. *Initiation phase and MCS value*

For the simulation with the dynamic value of the MCS, and without pre-delamination, the initial main delamination does not appear (Fig. 17a) whereas it appears for the simulation with the quasi-static value of the MCS (Fig. 17b). The position of the initial main delamination seems chaotic in simulations but also, to a lesser extent, in experiment (Fig. 5) thus we will not confront position of the main initial delamination neither its timing.

During experiments and simulations, the initial main delamination seems to be the tipping point of the initial phase, initiating the force decrease of the initial main peak.

During the initiation phase, simulations with dynamic MCS and without natural initial main delamination are not representative of experiments, especially on the force–displacement curve. On the contrary, the force–displacement curve of the simulation with the quasi-static value of the Mean Crushing Stress is representative of the experiment (Fig. 18).

5.2.3. *Main column formation and initial main delamination*

Simulated standard specimen's geometry does not initiate an initial main delamination and generates a main column on the right side whereas simulated specimens with an artificial initial main delamination generate a main column on the left side. This matches the experimental scenario where the initial main delamination is followed by a main column on the left side. Only the P5-4 specimen did not generate an initial main delamination during the experiment and had an unstable main column on the right side, like the normal simulated geometry. Therefore, the occurrence and the position of the initial main delamination is crucial to the morphology generated during the transition phase and sustained during the permanent phase.

The velocity effect on Mean Crushing Stress is crucial to the occurrence of the initial main delamination which is in turn crucial to the morphology of the permanent phase, thus to the average force level and the stability of the force plateau.

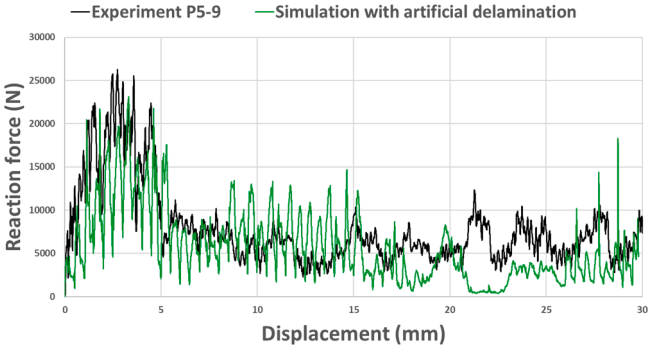

Fig. 15. Force-displacement curves of the pre-delaminated simulation and the P5-9 experiment (3D model, 30 mm of crushing, MCS = 140 MPa).

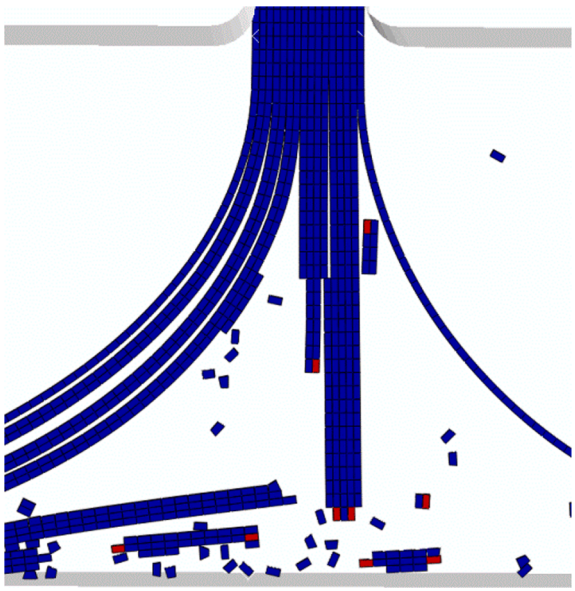

Fig. 16. Typical morphology of the expected steady phase for pseudo-2D simulation without artificial delamination, MCS = 140 MPa (to be compa**red with** Fig. 14).

5.2.4. *Fragmentation in the main column versus splaying initiation*

Experimental and simulated transversal expansion in crushed plies initiates a delamination and a slight lateral sliding on the base plate of exterior plies of the main column. Then, competition between bending and delamination propagation criteria determines if this slight lateral sliding will induce a macroscopic splaying of these sliding plies or an early bending fracture (source of macroscopic debris). The friction at the tip of the sliding plies is also of first importance in this competition.

During the steady phase, the main column occasionally loses some external plies to generate viable splaying plies and on the contrary bending occasionally fractures splaying plies to enlarge sustainably the main column.

5.2.5. *Importance of delamination sensitivity*

Considering splaying, experimental and simulated morphologies match very well, showing a good restitution of delamination sensitivity and initiation mechanisms. Splaying initiation and robustness are regulating the number of plies in the main column hence the crushing force levels too.

Sometimes, macroscopic buckling of the main column occurs, generating dramatic force gaps during crushing. Buckling is driven by the main column length, the number of plies, the Mean Crushing Stress and the lack of geometrical symmetry in the orientation of plies. Right and left delaminations drive the main column length and therefore contribute to this major instability event.

5.2.6. *Dissipated energies*

The simulations shows good consistency of various energies (Fig. 19) as the same total dissipated energy is found with three methods: the area under the force–displacement curve (not extrapolated to a 60 mm width), the sum of sub-energies (friction, delamination, ply crushing/damage), the external work applied through boundary conditions. Only the sum of sub-energies is represented in Fig. 19. In particuler the "Distortion Control" tool and the default numerical viscosity of Abaqus Explicit, used to respectively reduce excessive distortion of volume elements and to smooth the stress waves, were not plotted in this figure because their contribution is negligible; confirming their using is acceptable from a point of view of the dissipated energy.

As expected, most of the dissipated energy comes from the crushing of volume elements and a substantial energy also comes from friction.

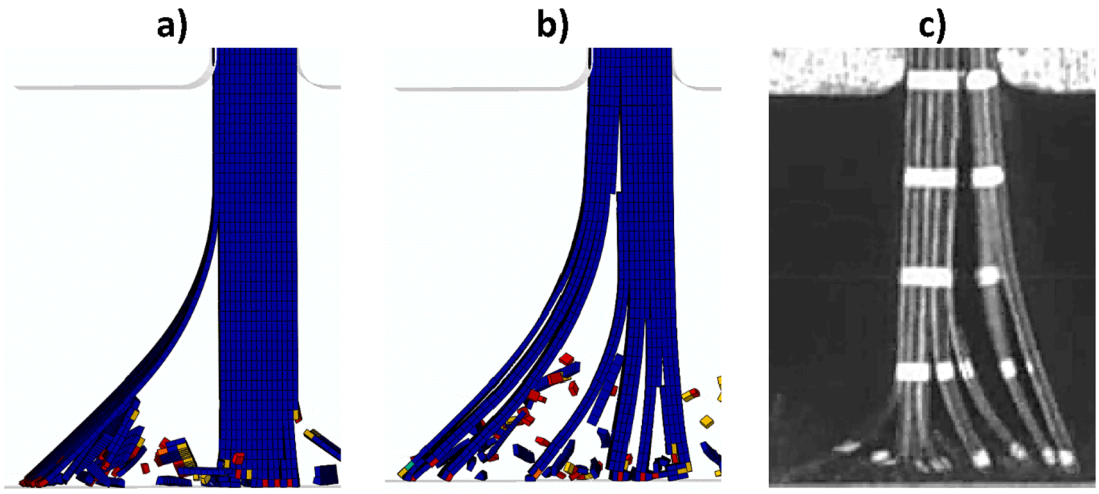

Fig. 17. Morphologies showing eventual initial main delamination for: a) simulation with dynamic MCS at d = 5.1 mm b) simulation with quasi-static MCS at d = 5.1 mm c) experiment P5-9 at d = 4.1 mm.

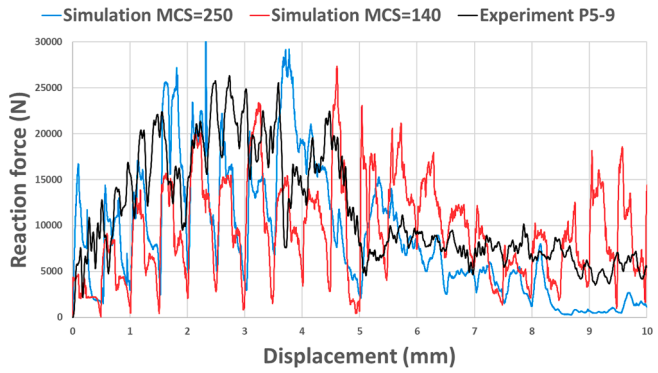

Fig. 18. Force-displacement curves on the first 10 mm of crushing. Neither of both simulations is artificially delaminated and each has a different value of Mean Crushing Stress (quasi-static. 250 MPa, dynamic. 140 MPa).

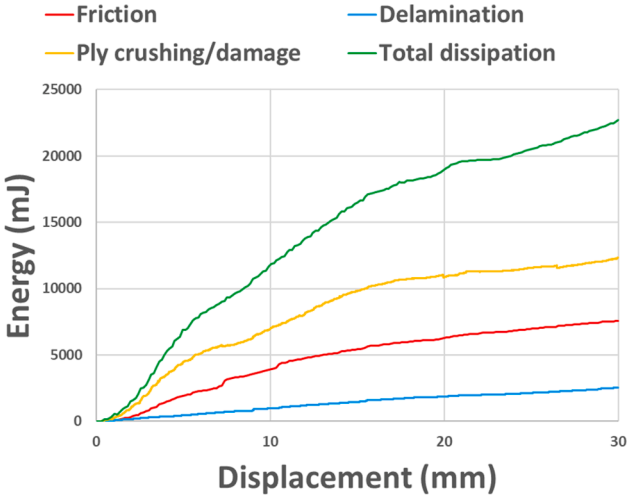

Fig. 19. Dissipated energies through various mechanisms during a simulation (3D model with artificial delamination, dynamic MCS, 8 mm width: energy not extrapolated to 60 mm).

6. Conclusion

A 3D finite element model for unidirectional composite materials has been developed, at mesoscale, in order to represent damage and energy dissipation in the crushing of composite structures. It has been applied to the crushing of laminated plates, a complex problem as it induces most of the mechanisms involved in crushing: delamination, splaying plies, failure in bending, localised crushing, debris wedges… The model has proven to be able to represent those mechanisms at mesoscale and thus to obtain realistic morphologies of the crushing front. Moreover, it solves the problem of stability of columns of plies under compression at constant stress observed in the tests and that the pseudo-2D former version of the model was not able to do.

Different parameters have been studied in order to see their influence and to understand the key points of the morphology main features and evolution, which define the global crushing force and thus the specific energy absorption of the structure.

The key points identified are:

- the stability, function of the specimen width: 3D simulations superior to pseudo-2D,
- the stability of the main column: highly sensitive to the delamination strengths and friction with the crushing plate,
- the tipping point of the initial main delamination on the morphology of the permanent phase and its relation to the Mean Crushing Stress velocity effects.

This last point should be experimentally investigated to obtain reliable values of this determining parameter.

CRediT authorship contribution statement

Florent Grotto: Conceptualization, Methodology, Software, Validation, Formal analysis, Investigation, Data curation, Writing – original draft. **Samuel Rivallant:** Conceptualization, Methodology, Validation, Formal analysis, Investigation, Resources, Data curation, Writing – original draft, Writing – review & editing, Supervision. **Christophe Bouvet:** Conceptualization, Methodology, Software, Validation, Formal analysis, Investigation, Resources, Data curation, Writing – original draft, Writing – review & editing, Supervision, Project administration, Funding acquisition.

Declaration of Competing Interest

The authors declare that they have no known competing financial interests or personal relationships that could have appeared to influence the work reported in this paper.

Acknowledgements

This study was founded by Région Occitanie (France) and BPIFrance in the framework of the project PLUME S3L which partners: Stelia Aerospace, ICA (ISAE-SUPAERO and Université Paul Sabatier de Toulouse), AKKA, CELSO, RESCOLL, CETIM, ALTAIR, AXYAL and EROC.

This project also benefited from the resources of the CALMIP supercomputer (project 2018-P1017).

References

[1] Bambach MR. Axial capacity and crushing of thin-walled metal, fibre–epoxy and composite metal–fibre tubes. Thin-Walled Struct 2010;48:440–52.
[2] Ramakrishna S. Microstructural design of composite materials for crashworthy structural applications. Mat Design 1997;18(3):167–73.
[3] Farley GL, Jones RM. Energy-absorption capability of composite tubes and beams. NASA TM-101634; 1989.
[4] Palanivelu S, Van Paepegem W, Degrieck J, Kakogiannis D, Van Ackeren J, Van Hemelrijck D, et al. Comparative study of the quasi-static energy absorption of small-scale composite tubes with different geometrical shapes for use in sacrificial cladding structures. Polym Test 2010;29(3):381–96.
[5] Jiménez MA, Miravete A, Larrodé E, Revuelta D. Effect of trigger geometry on energy absorption in composite profiles. Compos Struct 2000;48(1-3):107–11.
[6] Costa S, Fagerström M, Olsson R. Development and validation of a finite deformation fibre kinking model for crushing of composites. Compos Sci Technol 2020;197:108236.
[7] Hull D. A unified approach to progressive crushing of fiber reinforced tubes. Compos Sci and Technol 1991;40:377–421.
[8] McGregor C, Vaziri R, Xiao X. Finite element modelling of the progressive crushing of braided composite tubes under axial impact. Int J Impact Eng 2010;37(6):662–72.
[9] Yang X, Ma J, Wen D, Yang J. Crashworthy design and energy absorption mechanisms for helicopter structures: a systematic literature review. Prog Aerosp Sci 2020;114:100618. https://doi.org/10.1016/j.paerosci.2020.100618.
[10] Dalli D, Varandas LF, Catalanotti G, Foster S, Falzon BG. Assessing the current modelling approach for predicting the crashworthiness of Formula One composite structures. Compos B 2020;201:108242.
[11] Nixon S, Barnes G. Effective crushing simulation for composite structures. ICCM-17, Edinburgh, UK; July 2009.
[12] Feraboli P, Wade B, Deleo F, Rassaian M, Higgins M, Byar A. LS-DYNA MAT54 modeling of the axial crushing of a composite tape sinusoidal specimen. Compos A 2011;42(11):1809–25.
[13] Oshkovr SA, Taher ST, Oshkour AA, Ariffin AK, Azhari CH. Finite element modelling of axially crushed silk/epoxy composite square tubes. Compos Struct 2013;95:411–8.
[14] Cherniaev A, Butcher C, Montesano J. Predicting the axial crush response of CFRP tubes using three damage-based constitutive models. Thin-Walled Struct 2018;129:349–64.
[15] Zhu G, Sun G, Li G, Cheng A, Li Q. Modeling for CFRP structures subjected to quasi-static crushing. Compos Struct 2018;184:41–55.
[16] Pinho ST, Camanho PP, de Moura MF. Numerical simulation of the crushing process of composite materials. Int J Crashworthiness 2004;9(3):263–76.
[17] McCarthy MA, Wiggenraad JFM. Numerical investigation of a crash test of a composite helicopter subfloor structure. Compos Struct 2001;51(4):345–59.
[18] Liu Q, Lin Y, Zong Z, Sun G, Li Q. Lightweight design of carbon twill weave fabric composite body structure for electric vehicle. Compos Struct 2013;97:231–8.
[19] Joosten MW, Dutton S, Kelly D, Thomson R. Experimental and numerical investigation of the crushing response of an open section composite energy absorbing element. Compos Struct 2011;93(2):682–9.
[20] Palanivelu S, Van Paepegem W, Degrieck J, Van Ackeren J, Kakogiannis D, Wastiels J, et al. Parametric study of crushing parameters and failure patterns of pultruded composite tubes using cohesive elements and seam: Part II – Multiple delaminations and initial geometric imperfections. Polym Test 2010;29(7):803–14.
[21] Sokolinsky VS, Indermuehle KC, Hurtado JA. Numerical simulation of the crushing process of a corrugated composite plate. Compos A 2011;42(9):1119–26.
[22] Alkhatib F, Mahdi E, Dean A. Crushing response of CFRP and KFRP composite corrugated tubes to quasi-staticslipping axial loading: experimental investigation and numerical simulation. Compos Struct 2020;246:112370. https://doi.org/10.1016/j.compstruct.2020.112370.
[23] Zhou G, Sun Q, Fenner J, Li D, Zeng D, Su X. Crushing behaviors of unidirectional carbon fiber reinforced plastic composites under dynamic bending and axial crushing loading. Int J Impact Eng 2020;140:103539.
[24] Zhang JunYuan, Bingquan Lu, Zheng D, Li Z. Experimental and numerical study on energy absorption performance of CFRP/aluminum hybrid square tubes under axial loading. Thin-Walled Struct 2020;155:106948.
[25] Liu Q, Jie Fu, Ma Y, Zhang Y, Li Q. Crushing responses and energy absorption behaviors of multi-cell. Thin-Walled Struct 2020;155:106930.
[26] Han X, Hou S, Ying L, Hou W, Aliyev H. On the fracture behaviour of adhesively bonded CFRP hat-shaped thin-walled beam under axial crushing load: an experimental and modelling study. Compos Struct 2019;215:258–65.
[27] Mahbod M, Asgari M. Energy absorption analysis of a novel foam-filled corrugated composite tube under axial and oblique loadings. Thin-Walled Struct 2018;129:58–73.
[28] Chiu LNS, Falzon BG, Boman R, Chen B, Yan W. Wenyi Yan. Finite element modelling of composite structures under crushing load. Compos Struct 2015;131:215–28.
[29] Liu H, Falzon BG, Dear JP. An experimental and numerical study on the crush behaviour of hybrid unidirectional/woven carbon-fibre reinforced composite laminates. Int J Mech Sci 2019;164:105160.
[30] McGregor C, Zobeiry N, Vaziri R, Poursartip A, Xiao X. Calibration and validation of a continuum damage mechanics model in aid of axial crush simulation of braided composite tubes. Compos: Part A 2017;95:208–19.
[31] Rondina F, Donati L. Comparison and validation of computational methods for the prediction of the compressive crush energy absorption of CFRP structures. Compos Struct 2020;254:112848.
[32] Ladevèze P, Allix O, Gornet L, Lévêque D, Perret L. A computational damage mechanics approach for laminates: identification and comparison with experimental results. Stud Appl Mech 1998;46:481–500.
[33] Pineda EJ, Waas AM. Numerical implementation of a multiple-ISV thermodynamically-based work potential theory for modeling progressive damage and failure in fiber-reinforced laminates. Int J Fract 2013;182(1):93–122.
[34] Israr HA, Rivallant S, Bouvet C, Barrau JJ. Finite element simulation of 0°/90° CFRP laminated plates subjected to crushing using a free-face-crushing concept. Compos Part Appl Sci Manuf 2014;62:16–25.
[35] Israr HA, Rivallant S, Barrau JJ. Experimental investigation on mean crushing stress characterization of carbon–epoxy plies under compressive crushing mode. Compos Struct 2013;96:357–64.
[36] Duong AV, Rivallant S, Barrau J-J, et al. Influence of speed on the crushing behavior of composite plates. In: ACCM 7 – 7th Asian-Australasian Conference on Composite Materials; 2010.
[37] Guillon D. Etude des mécanismes d'absorption d'énergie lors de l'écrasement progressif de structures composites à base de fibre de carbone [Ph.D Thesis]. ISAE; Université de Toulouse; 2008.
[38] Guillon D, Rivallant S, Barrau J, et al. Experimental and numerical study of the splaying mode crush of CFRP laminates. ICCM 17–17th International Conference on Composite Materials. 2009.
[39] Bouvet C, Rivallant S, Barrau JJ. Low velocity impact modeling in composite laminates capturing permanent indentation. Compos Sci Technol 2012;72(16):1977–88.
[40] Adam L, Bouvet C, Castanié B, Daidié A, Bonhomme E. Discrete ply model of circular pull-through test of fasteners in laminates. Compos Struct 2012;94(10):3082–91.
[41] Rivallant S, Bouvet C, Hongkarnjanakul N. Failure analysis of CFRP laminates subjected to compression after impact: FE simulation using discrete interface elements. Composites: Part A 2013;55:83–93.